



**HAL**  
open science

# A unified formulation of quasi-geostrophic and shallow water equations via projection

Louis Thiry, Long Li, Etienne Mémin, Guillaume Roulet

► **To cite this version:**

Louis Thiry, Long Li, Etienne Mémin, Guillaume Roulet. A unified formulation of quasi-geostrophic and shallow water equations via projection. *Journal of Advances in Modeling Earth Systems*, 2024, <https://doi.org/10.1029/2024MS004510> . hal-04673756v2

**HAL Id: hal-04673756**

**<https://hal.science/hal-04673756v2>**

Submitted on 27 Sep 2024

**HAL** is a multi-disciplinary open access archive for the deposit and dissemination of scientific research documents, whether they are published or not. The documents may come from teaching and research institutions in France or abroad, or from public or private research centers.

L'archive ouverte pluridisciplinaire **HAL**, est destinée au dépôt et à la diffusion de documents scientifiques de niveau recherche, publiés ou non, émanant des établissements d'enseignement et de recherche français ou étrangers, des laboratoires publics ou privés.



Distributed under a Creative Commons Attribution 4.0 International License

# A unified formulation of quasi-geostrophic and shallow water equations via projection

Louis Thiry<sup>1</sup>, Long Li<sup>2</sup>, Etienne Mémin<sup>2</sup>, and Guillaume Roullet<sup>3</sup>

<sup>1</sup>ANGE Team, INRIA Paris, Laboratoire Jacques-Louis Lions, Sorbonne University, France

<sup>2</sup>ODYSSEY Team, INRIA Rennes, IRMAR, University of Rennes I, France

<sup>3</sup>Laboratoire d'Océanographie Physique et Spatiale, Université de Bretagne Occidentale, Brest, France

## Key Points:

- Introduces QG equations as a projection of RSW equations using the same prognostic variables.
- Allows consistent nested numerical methods for both QG and RSW equations.
- Successfully tested on vortex shear instability, double-gyre circulation, and a simplified North Atlantic configuration.

---

Corresponding author: Long Li, [long.li@inria.fr](mailto:long.li@inria.fr)

**Abstract**

This paper introduces a unified model for layered rotating shallow-water (RSW) and quasi-geostrophic (QG) equations, based on the intrinsic relationship between these two sets of equations. We propose a novel formulation of the QG equations as a projection of the RSW equations. This formulation uses the same prognostic variables as RSW, namely velocity and layer thickness, thereby restoring the proximity of these two sets of equations. It provides direct access to the ageostrophic velocities embedded within the geostrophic velocities resolved by the QG equations. This approach facilitates the study of differences between QG and RSW using a consistent numerical discretization. We demonstrate the effectiveness of this formulation through examples including vortex shear instability, double-gyre circulation, and a simplified North Atlantic configuration.

**Plain Language Summary**

In this paper, we present a straightforward way to connect two important sets of ocean equations: the layered rotating shallow-water (RSW) equations and the quasi-geostrophic (QG) equations. We consider a unified method to formulate the QG equations as a projection of the RSW equations. This method uses the same variables as the RSW equations, making it easier to understand how these two sets of equations relate to each other. Our approach also provides direct access to important velocity information that is usually hidden in the QG equations. This allows us to study the differences between the QG and RSW equations using the same numerical techniques. We show the benefits of our model with two examples: a vortex shear instability and a double-gyre configuration. This work provides a useful tool for the understanding of ocean dynamics. Developing a unified numerical framework for nested models can greatly simplify oceanographic modeling and enhance accuracy.

**1 Introduction**

Large-scale ocean models offer a natural trade-off between complexity and realism. On one side, the primitive equations (PE) are sufficiently realistic for climate simulations and real-world data assimilation. However, they are quite complex as they describe the coupling between the equations of motion (mass and momentum) and the conservation of tracers via the equation of state following thermodynamic laws. On the other side, the barotropic planetary geostrophic equations can be efficiently solved with a single prognostic variable (the thickness), yet they ignore thermodynamics and vertical variations.

Between these extremes, there exist approximate models of the PE, such as the multi-layer rotating shallow-water (RSW) and the multi-layer quasi-geostrophic (QG) models. The latter can be either derived from the former using an asymptotic approach (Pedlosky, 2013; Vallis, 2017) or considered as a vertical discretization of the continuously stratified QG model derived from the PE. These layered models describe the dynamics of vertically stratified flow in isentropic (or isopycnal) coordinates and only require solving the horizontal momentum and mass equations. For instance, the multi-layer RSW model can fairly reproduce the ocean dynamics in the Gulf Stream region with only five vertical levels (Hurlburt & Hogan, 2000). The multi-layer QG equations are widely adopted for the development of deterministic mesoscale eddy parameterizations (Marshall et al., 2012; Jansen & Held, 2014; Bachman et al., 2017; Uchida et al., 2022) as well as stochastic ones (Berloff, 2005; Grooms et al., 2015; Zanna et al., 2017; Bauer et al., 2020; Li et al., 2023). These two sets of equations can be used as research tools since their numerical integration is light enough to run on laptop computers.

Although the multi-layer QG equations are formally derived from the multi-layer RSW equations, their relationship is still not clear from a numerical point of view. Indeed, they are usually written with different prognostic variables. The prognostic variables of the RSW system are the horizontal velocity ( $\mathbf{u}, \mathbf{v}$ ) and the layer thickness  $\mathbf{h}$ , whereas the QG system

62 is typically formulated with potential vorticity  $\mathbf{q}$  as the single prognostic variable, from  
 63 which one can diagnose the streamfunction  $\psi$  and the pressure  $\mathbf{p}$ . This difference breaks  
 64 the conceptual continuity between these two equation sets in the ocean model hierarchy and  
 65 brings some undesirable consequences in practice. For instance, many eddy parameteriza-  
 66 tions (e.g., Bachman, 2019; Li et al., 2023) yield different formulations and/or discretizations  
 67 when applied to the RSW model using the horizontal velocity  $(\mathbf{u}, \mathbf{v}, \mathbf{h})$  and layer thickness  
 68 as the prognostic variables, or to the QG model using potential vorticity  $\mathbf{q}$  as the prognostic  
 69 variable. Moreover, from a practical point of view, it is not straightforward to use the same  
 70 discrete schemes for these two different models in order to compare them under the same  
 71 configuration.

72 In this work, we propose to reformulate the multi-layer QG model using horizontal  
 73 velocity and layer thickness  $(\mathbf{u}, \mathbf{v}, \mathbf{h})$  as prognostic variables. This unified reformulation is  
 74 achieved by expressing the QG equations as a projection of the RSW equations. We also  
 75 present a numerical algorithm to integrate the QG equations corresponding to the proposed  
 76 formulation. This projection approach allows for the construction of a QG discretization  
 77 on top of any RSW discretization. Moreover, this formulation provides direct access to the  
 78 ageostrophic velocity, which is hidden in the standard QG model formulation but contributes  
 79 to QG dynamics.

80 Similarly, the QG dynamics can be understood as a projection in the space of normal-  
 81 mode variables, as already proposed by Leith (1980); Salmon (1998); Saujani and Shepherd  
 82 (2006). This projection reveals that the slow modes correspond to the linearized potential  
 83 vorticity of the RSW model, while the fast modes are associated with the ageostrophic curl  
 84 and divergence components. However, this formal analysis relies on Fourier transformation,  
 85 which assumes periodic solutions and thereby limits numerical development. In our for-  
 86 mulation, the QG equations are considered as a projection of the RSW model in physical  
 87 space. This approach is independent of the model configuration, such as the shape of the  
 88 boundary. It provides a consistent framework for developing the corresponding numerical  
 89 scheme in realistic basins.

90 For the numerical experiments, we adopt the RSW discretization proposed by Roulet  
 91 and Gaillard (2022), which relies on the vector invariant formulation and an advanced  
 92 high-order WENO advection scheme. The discretized QG model uses the same dynamical  
 93 core as the multi-layer RSW model, with the only modification being the addition of the  
 94 projection operator. We developed a compact, efficient, and CPU/GPU portable Python  
 95 code using the PyTorch library (Paszke et al., 2019). We first use a simple test case of vortex  
 96 shear instability to investigate the similarities and differences of the QG and RSW solutions  
 97 according to different Rossby numbers. We then study the solutions produced by QG and  
 98 RSW in an idealized wind-driven double-gyre configuration. This final configuration is  
 99 also implemented in the North Atlantic basin with simplified lateral and vertical boundary  
 100 conditions.

101 This paper is organized as follows. In Section 2, we briefly recall the derivation of the  
 102 multi-layer RSW and QG equations. In Section 3, we present our projected QG formulation.  
 103 In Section 4, we numerically test our formulation on different configurations. We conclude  
 104 and discuss further perspectives in Section 5.

## 105 2 Multi-layer RSW and QG equations

106 In this section, we first review the governing equations of the RSW system. We then  
 107 briefly explain the QG scaling of the RSW equations and present the standard multi-layer  
 108 QG equations, using potential vorticity  $\mathbf{q}$  as the prognostic variable.

## 2.1 Multi-layer RSW equations

The stratification of a multi-layer RSW model consists of a stack of  $n$  isopycnal layers, as illustrated in Figure 1 with  $n = 3$  layers. By convention, we index the layers from  $i = 1$  for the top layer to  $i = n$  for the bottom layer. These layers have a uniform reference thickness  $H_i$  and a density  $\rho_i$ . As shown in Figure 1, the total thickness of a layer  $i$  is the sum of the reference thickness  $H_i$  and the thickness anomaly  $h_i(x, y)$ . The vertical interface displacement  $\eta_i(x, y)$  and the hydrostatic pressure  $p_i(x, y)$  are given by

$$\eta_i = \sum_{j=i}^n h_j, \quad p_i = \rho_1 \sum_{j=1}^i g'_j \eta_j. \quad (1)$$

For  $i > 1$ , the reduced gravities are  $g'_i = g(\rho_i - \rho_{i-1})/\rho_1$ , and for the top layer  $g'_1 = g$ .

Using the following vector notation

$$\mathbf{H} = (H_1, \dots, H_n), \quad (2a)$$

$$\mathbf{h} = (h_1(x, y), \dots, h_n(x, y)), \quad (2b)$$

$$\boldsymbol{\eta} = (\eta_1(x, y), \dots, \eta_n(x, y)), \quad (2c)$$

$$\mathbf{p} = (p_1(x, y), \dots, p_n(x, y)), \quad (2d)$$

we can rewrite the linear relations between  $\mathbf{h}$ ,  $\boldsymbol{\eta}$  and  $\mathbf{p}$  in a compact form

$$\mathbf{h} = \text{diag}(\mathbf{H})\mathbf{A}\mathbf{p}, \quad (3a)$$

$$\boldsymbol{\eta} = \mathbf{C}\mathbf{h}, \quad (3b)$$

$$\mathbf{p} = \mathbf{M}\mathbf{h}, \quad (3c)$$

with the matrices

$$A = \frac{1}{\rho_1} \begin{bmatrix} \frac{1}{H_1 g'_1} + \frac{1}{H_1 g'_2} & \frac{-1}{H_1 g'_2} & \cdot & \cdot \\ \frac{-1}{H_2 g'_2} & \frac{1}{H_2} \left( \frac{1}{g'_2} + \frac{1}{g'_3} \right) & \frac{-1}{H_2 g'_3} & \cdot \\ \cdot & \cdot & \cdot & \cdot \\ \cdot & \cdot & \frac{-1}{H_n g'_n} & \frac{1}{H_n g'_n} \end{bmatrix}, \quad (3d)$$

$$B = \rho_1 \begin{bmatrix} g'_1 & 0 & 0 & \dots & 0 \\ g'_1 & g'_2 & 0 & \dots & 0 \\ \cdot & \cdot & \cdot & \cdot & \cdot \\ g'_1 & g'_2 & g'_3 & \dots & g'_n \end{bmatrix}, \quad C = \begin{bmatrix} 1 & 1 & \dots & 1 & 1 \\ 0 & 1 & \dots & 1 & 1 \\ \cdot & \cdot & \cdot & \cdot & \cdot \\ 0 & 0 & \dots & 0 & 1 \end{bmatrix}, \quad (3e)$$

and  $M = BC$ . We then introduce the velocity components  $(\mathbf{u}, \mathbf{v})$ , the kinetic energy  $\mathbf{k}$ , and the relative vorticity  $\boldsymbol{\omega}$ :

$$\mathbf{u} = (u_1(x, y), \dots, u_n(x, y)), \quad (4a)$$

$$\mathbf{v} = (v_1(x, y), \dots, v_n(x, y)), \quad (4b)$$

$$\mathbf{k} = (\mathbf{u}^2 + \mathbf{v}^2)/2, \quad (4c)$$

$$\boldsymbol{\omega} = \partial_x \mathbf{v} - \partial_y \mathbf{u}. \quad (4d)$$

With these variables, the multi-layer RSW equations read

$$\partial_t \mathbf{u} = (\boldsymbol{\omega} + f)\mathbf{v} - \partial_x(\mathbf{p} + \mathbf{k}), \quad (5a)$$

$$\partial_t \mathbf{v} = -(\boldsymbol{\omega} + f)\mathbf{u} - \partial_y(\mathbf{p} + \mathbf{k}), \quad (5b)$$

$$\partial_t \mathbf{h} = -\mathbf{H}(\partial_x \mathbf{u} + \partial_y \mathbf{v}) - \partial_x(\mathbf{u}\mathbf{h}) - \partial_y(\mathbf{v}\mathbf{h}), \quad (5c)$$

where  $f$  is the Coriolis parameter. These equations can be formulated in the compact form

$$\partial_t \mathbf{X} = F(\mathbf{X}), \quad (6a)$$

142 with  $\mathbf{X} = (\mathbf{u}, \mathbf{v}, \mathbf{h})^T$ , the state variable, and

$$143 \quad F \begin{pmatrix} \mathbf{u} \\ \mathbf{v} \\ \mathbf{h} \end{pmatrix} = \begin{pmatrix} (\partial_x \mathbf{v} - \partial_y \mathbf{u} + f)\mathbf{v} - \partial_x (M\mathbf{h} + (\mathbf{u}^2 + \mathbf{v}^2)/2) \\ -(\partial_x \mathbf{v} - \partial_y \mathbf{u} + f)\mathbf{u} - \partial_y (M\mathbf{h} + (\mathbf{u}^2 + \mathbf{v}^2)/2) \\ -\mathbf{H}(\partial_x \mathbf{u} + \partial_y \mathbf{v}) - \partial_x(\mathbf{u}\mathbf{h}) - \partial_y(\mathbf{v}\mathbf{h}) \end{pmatrix}, \quad (6b)$$

144 the RSW model operator.

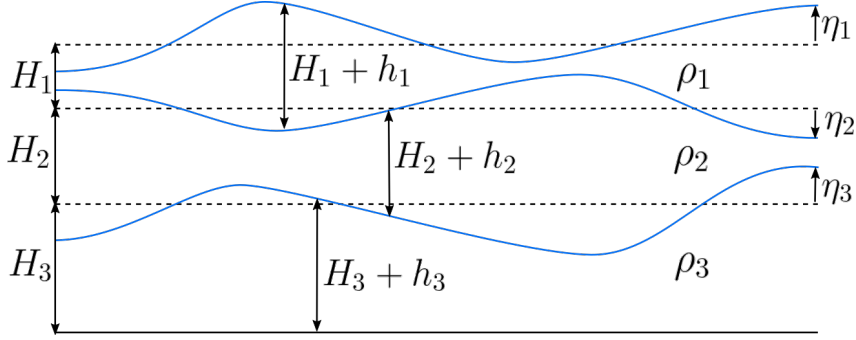


**Figure 1.** Vertical cross-section of a three-layer RSW model displaying layer thicknesses  $H_i + h_i$  and interface heights  $\eta_i$

## 145 2.2 QG scaling of RSW equations

146 The QG model is derived from the RSW model under two scaling assumptions:  $Ro \ll 1$   
 147 and  $Bu \sim 1$  (J. McWilliams, 2006; Zeitlin, 2018), where  $Ro$  is the Rossby number and  $Bu$   
 148 is the Burger number (ratio of the deformation Radius  $L_d = \sqrt{gH}/f$  to the scale of motion  $L$ ).  
 149 The consistency of the QG scaling necessitates a beta-plane approximation for the Coriolis  
 150 parameter  $f = f_0 + \beta y$ , where  $\beta$  is the meridional gradient of the Coriolis parameter. The  
 151 condition  $Ro \ll 1$  implies that the velocity is near the geostrophic balance, specifically that  
 152 the ageostrophic correction is  $O(Ro)$ . We define  $(\mathbf{u}_g, \mathbf{v}_g)$  as the geostrophic velocity that  
 153 adheres the geostrophic balance

$$154 \quad -f_0 \mathbf{u}_g = \partial_y \mathbf{p}, \quad f_0 \mathbf{v}_g = \partial_x \mathbf{p}, \quad (7a)$$

155 and decompose the velocity into the geostrophic and the ageostrophic components  $(\mathbf{u}_a, \mathbf{v}_a)$ :

$$156 \quad \mathbf{u} = \mathbf{u}_g + \mathbf{u}_a, \quad \mathbf{v} = \mathbf{v}_g + \mathbf{v}_a. \quad (7b)$$

157 The conditions  $Bu \sim 1$  and  $Ro \ll 1$  imply that  $\mathbf{h}/\mathbf{H} \sim O(Ro)$ . Following the approach of  
 158 Holton (1973); J. McWilliams (2006); Cushman-Roisin and Beckers (2011); Zeitlin (2018),  
 159 we do not decompose  $\mathbf{p}, \mathbf{h}, \boldsymbol{\eta}$  into a geostrophic and an ageostrophic parts, as this would  
 160 require an additional assumption to define the ageostrophic component of the stratification,  
 161 which is unnecessary for deriving the QG model. Thus, there is a single mass variable and  
 162 two velocity components per layer.

163 Under these assumptions, the multi-layer QG equations can be expressed in terms of  
 164 three equations for the prognostic variables  $(\mathbf{u}_g, \mathbf{v}_g, \mathbf{h})$  with the right-hand side terms that  
 165 depend on the ageostrophic velocities  $(\mathbf{u}_a, \mathbf{v}_a)$ :

$$166 \quad \partial_t \mathbf{u}_g = (\boldsymbol{\omega}_g + f_0 + \beta y)\mathbf{v}_g + f_0 \mathbf{v}_a - \partial_x (M\mathbf{h} + \mathbf{k}_g), \quad (8a)$$

$$167 \quad \partial_t \mathbf{v}_g = -(\boldsymbol{\omega}_g + f_0 + \beta y)\mathbf{u}_g - f_0 \mathbf{u}_a - \partial_y (M\mathbf{h} + \mathbf{k}_g), \quad (8b)$$

$$168 \quad \partial_t \mathbf{h} = -\mathbf{H}(\partial_x \mathbf{u}_g + \partial_y \mathbf{v}_g) - \partial_x(\mathbf{u}_g \mathbf{h}) - \partial_y(\mathbf{v}_g \mathbf{h}) - \mathbf{H}(\partial_x \mathbf{u}_a + \partial_y \mathbf{v}_a). \quad (8c)$$

169 Note that using the geostrophic balance (7a), one can simplify these equations to

$$170 \quad \partial_t \mathbf{u}_g = (\boldsymbol{\omega}_g + \beta y) \mathbf{v}_g + f_0 \mathbf{v}_a - \partial_x \mathbf{k}_g, \quad (9a)$$

$$171 \quad \partial_t \mathbf{v}_g = -(\boldsymbol{\omega}_g + \beta y) \mathbf{u}_g - f_0 \mathbf{u}_a - \partial_y \mathbf{k}_g, \quad (9b)$$

$$172 \quad \partial_t \mathbf{h} = -\partial_x(\mathbf{u}_g \mathbf{h}) - \partial_y(\mathbf{v}_g \mathbf{h}) - \mathbf{H}(\partial_x \mathbf{u}_a + \partial_y \mathbf{v}_a). \quad (9c)$$

173 In this form, the QG equations still appear similar to the RSW equations, but this is  
 174 misleading as there is only one degree of freedom per layer. The two components of the  
 175 geostrophic velocity are constrained by  $\mathbf{h}$  via (7a) and (3a). Another difficulty with this  
 176 system is that, although well-posed, it is highly implicit. There is no straightforward method  
 177 to determine the ageostrophic velocity. In practice, and particularly for numerical models,  
 178 the equations are rewritten in a more explicit form. This form reveals a hidden variable of  
 179 the system that is the potential vorticity (PV):

$$180 \quad \mathbf{q} = \beta y + \boldsymbol{\omega}_g - f_0 \frac{\mathbf{h}}{\mathbf{H}}. \quad (10)$$

### 181 2.3 Multi-layer QG equations

182 The multi-layer QG equations are obtained upon by differentiating (10) with respect  
 183 to time and utilizing (9). The resulting equations are

$$184 \quad \partial_t \mathbf{q} = -\partial_x(\mathbf{u}_g \mathbf{q}) - \partial_y(\mathbf{v}_g \mathbf{q}), \quad (11a)$$

$$185 \quad \Delta \mathbf{p} - f_0^2 A \mathbf{p} = f_0 \mathbf{q} - f_0 \beta y, \quad (11b)$$

$$186 \quad -f_0 \mathbf{u}_g = \partial_y \mathbf{p}, \quad f_0 \mathbf{v}_g = \partial_x \mathbf{p}, \quad (11c)$$

187 where  $\Delta = \partial_{xx}^2 + \partial_{yy}^2$  denotes the horizontal Laplacian operator, and  $A$  represents the vertical  
 188 discretization of the stretching operator introduced in Equation (3d). The PV  $\mathbf{q}$  is the sole  
 189 prognostic variable in (11a). All other model variables are derived from  $\mathbf{q}$  via the diagnostic  
 190 relations (11b) for  $\mathbf{p}$  and (11c) for  $\mathbf{u}$  and  $\mathbf{v}$ . The QG model is thus expressed in terms of  
 191 the variables  $(\mathbf{q}, \mathbf{p})$ , with  $\mathbf{p}/f_0$  being the vector of streamfunction for each layer.

192 Numerical implementations of the QG model typically rely on this system of equations.  
 193 However, this system differs significantly from the RSW system of equations. One notable  
 194 aspect is the absence of the ageostrophic velocities from the RSW system of equations. This  
 195 absence does not imply that  $\mathbf{u}_a$  and  $\mathbf{v}_a$  vanish; rather, it means they can be disregarded if  
 196 the focus is solely on the evolution of  $\mathbf{p}$  and  $\mathbf{q}$ . The substantial difference between the QG  
 197 and RSW model equations complicates direct comparisons between them. Consequently,  
 198 numerical versions of the QG and RSW models generally have distinct implementations,  
 199 with differing numerical methods in all aspects. In the following sections, we demonstrate  
 200 how to reestablish the similarity between the two models.

## 201 3 Quasi-geostrophic model as projected rotating shallow-water

202 In this section, we propose a straightforward formulation of the QG equation using the  
 203 horizontal velocity and layer thickness  $(\mathbf{u}, \mathbf{v}, \mathbf{h})$  as state variables, along with the non-linear  
 204 RSW operator  $F$  defined in (6b), and a linear projection operator  $P$ . To our knowledge, this  
 205 projection relation has been largely overlooked, with one notable exception being Charve  
 206 (2004).

### 207 3.1 Projection formulation

208 To derive this projection, we start from the QG equations (8), and isolate the part  
 209 controlled by  $F$ :

$$210 \quad \partial_t \begin{pmatrix} \mathbf{u}_g \\ \mathbf{v}_g \\ \mathbf{h} \end{pmatrix} = F \begin{pmatrix} \mathbf{u}_g \\ \mathbf{v}_g \\ \mathbf{h} \end{pmatrix} + \begin{pmatrix} f_0 \mathbf{v}_a \\ -f_0 \mathbf{u}_a \\ -\mathbf{H}(\partial_x \mathbf{u}_a + \partial_y \mathbf{v}_a) \end{pmatrix}, \quad (12)$$

211 where several terms cancel due to the geostrophic balance. In this form, the QG model can  
 212 be interpreted as a RSW model applied to the geostrophic component and forced by an  
 213 ageostrophic source term, represented by the second term of the right-hand side.

214 Let us now introduce the PV linear operator  $Q$ :

$$215 \quad Q \begin{pmatrix} \mathbf{u} \\ \mathbf{v} \\ \mathbf{h} \end{pmatrix} = \partial_x \mathbf{v} - \partial_y \mathbf{u} - f_0 \frac{\mathbf{h}}{\mathbf{H}}. \quad (13a)$$

216 This operator relates to the PV by

$$217 \quad Q \begin{pmatrix} \mathbf{u}_g \\ \mathbf{v}_g \\ \mathbf{h} \end{pmatrix} = \mathbf{q} - \beta y, \quad (13b)$$

218 and ensures that the contribution of the ageostrophic source term in (12) vanishes:

$$219 \quad Q \begin{pmatrix} f_0 \mathbf{v}_a \\ -f_0 \mathbf{u}_a \\ -\mathbf{H}(\partial_x \mathbf{u}_a + \partial_y \mathbf{v}_a) \end{pmatrix} = 0. \quad (13c)$$

220 Since  $Q$  is independent of time, it commutes with the time derivative. Therefore,

$$221 \quad \partial_t Q \begin{pmatrix} \mathbf{u}_g \\ \mathbf{v}_g \\ \mathbf{h} \end{pmatrix} = Q \circ F \begin{pmatrix} \mathbf{u}_g \\ \mathbf{v}_g \\ \mathbf{h} \end{pmatrix}. \quad (14)$$

222 This equation is a reformulation of (11a), representing the conservation of PV. As  $Q$  reduces  
 223 the state vector from three to one variable, we need a reverse operation to retrieve the three  
 224 variables  $(\mathbf{u}_g, \mathbf{v}_g, \mathbf{h})$ . This is accomplished by introducing the geostrophic operator  $G$ :

$$225 \quad G(\mathbf{p}) = \begin{pmatrix} -\partial_y \mathbf{p} \\ \partial_x \mathbf{p} \\ f_0 \mathbf{H} A \mathbf{p} \end{pmatrix}. \quad (15a)$$

226 Thus,  $G$  is a linear operator with uniform and time-independent coefficients. The composi-  
 227 tion of the two operators  $Q$  and  $G$  yields:

$$228 \quad (Q \circ G)(\mathbf{p}) = \Delta \mathbf{p} - f_0^2 A \mathbf{p} \quad (15b)$$

229 which is the QG elliptic operator (11b) relating  $\mathbf{p}$  to  $\mathbf{q}$ . This operator is invertible (Dutton,  
 230 1974; Bourgeois & Beale, 1994), hence  $(Q \circ G)^{-1}$  is well-defined.

231 Finally, we introduce the QG projection operator  $P$ :

$$232 \quad P = G \circ (Q \circ G)^{-1} \circ Q. \quad (16)$$

233  $P$  is a projection because  $P \circ P = P$ , as demonstrated by

$$234 \quad P \circ P = G \circ (Q \circ G)^{-1} \circ (Q \circ G) \circ (Q \circ G)^{-1} \circ Q = P. \quad (17)$$

235 By construction,  $P$  preserves the geostrophic state  $\mathbf{X}_g = (\mathbf{u}_g, \mathbf{v}_g, \mathbf{h})^T$ , *i.e.*,  $P(\mathbf{X}_g) = \mathbf{X}_g$ .  
 236 Indeed, since  $\mathbf{X}_g$  is geostrophic, we have

$$237 \quad Q(\mathbf{X}_g) = \mathbf{q} - \beta y, \quad (18)$$

$$238 \quad (Q \circ G)^{-1}(\mathbf{q} - \beta y) = \mathbf{p}/f_0, \quad (19)$$

$$239 \quad G(\mathbf{p}/f_0) = \mathbf{X}_g. \quad (20)$$

240 Applying  $P$  to Equation (12), and noting that  $P$  commutes with  $\partial_t$ , we can formulate the  
 241 multi-layer QG model as

$$242 \quad \partial_t \mathbf{X}_g = P \circ F(\mathbf{X}_g). \quad (21)$$

243 This form differs from the RSW model (6a) by the additional projection operator  $P$  acting  
 244 on  $F$ . By projecting the RSW tendency onto the geostrophic manifold,  $P$  ensures that the  
 245 QG state remains in geostrophic balance. Alternatively, the QG model can be viewed as  
 246 evolving under the action of the RSW operator with the ageostrophic tendency removed.

247 To fully implement the projection method, it is necessary to specify the lateral boundary  
 248 condition for Equation (15b). The appropriate condition, consistent with the QG model, is  
 249 the Dirichlet boundary condition, where the pressure remains constant along each connected  
 250 boundary. Given that the projection is applied to the model tendency rather than the model  
 251 state, and that this work focuses on simply connected domains, the constant term is zero.  
 252 In cases involving multiply connected domains, the constant can be explicitly evaluated as  
 253 proposed by J. C. McWilliams (1977); however, this is beyond the scope of the present  
 254 paper.

### 255 3.2 Diagnostic variables

256 With this formulation, the ageostrophic velocity  $(\mathbf{u}_a, \mathbf{v}_a)$  can be expressed in a simple  
 257 closed form. Using equations (12) and (21), we have

$$258 \begin{pmatrix} f_0 \mathbf{v}_a \\ -f_0 \mathbf{u}_a \\ -\mathbf{H}(\partial_x \mathbf{u}_a + \partial_y \mathbf{v}_a) \end{pmatrix} = P \circ F \begin{pmatrix} \mathbf{u}_g \\ \mathbf{v}_g \\ \mathbf{h} \end{pmatrix} - F \begin{pmatrix} \mathbf{u}_g \\ \mathbf{v}_g \\ \mathbf{h} \end{pmatrix}. \quad (22)$$

259 In a numerical model, this requires only a basic difference between the QG and RSW  
 260 tendencies, with no costly computations.

261 Using this projection formulation, the QG system can be expressed with the same  
 262 prognostic variables as the RSW system, namely the horizontal velocity  $(\mathbf{u}, \mathbf{v})$  and the  
 263 layer thickness  $\mathbf{h}$ . This reestablishes the proximity between these two sets of equations  
 264 in the ocean model hierarchy, leading to four practical implications. First, given a RSW  
 265 discretization, one can implement the projection to derive the companion QG model for this  
 266 specific discretization. Second, this formulation provides access to the ageostrophic velocity  
 267 hidden in the QG equations at the cost of a simple subtraction. This enables an *a posteriori*  
 268 diagnostic of the validity of the QG scaling. For a given geostrophic state  $(\mathbf{u}_g, \mathbf{v}_g, \mathbf{h})$ , the  
 269 corresponding ageostrophic velocity  $(\mathbf{u}_a, \mathbf{v}_a)$  can be computed and checked against:

$$270 \frac{\mathbf{k}_a}{\mathbf{k}_g} \sim Ro^2, \quad \frac{\mathbf{h}}{\mathbf{H}} \sim Ro, \quad (23)$$

271 where  $\mathbf{k}_a = (|\mathbf{u}_a|^2 + |\mathbf{v}_a|^2)/2$  and  $\mathbf{k}_g = (|\mathbf{u}_g|^2 + |\mathbf{v}_g|^2)/2$  are the ageostrophic and the  
 272 geostrophic kinetic energies, respectively.

273 Third, using the same variables  $(\mathbf{u}, \mathbf{v}, \mathbf{h})$  facilitates the development of eddy parameter-  
 274 izations, such as those in Bachman (2019); Li et al. (2023), which work similarly for both the  
 275 RSW and the QG models. Finally, this formulation may offer new insights and approaches  
 276 for the mathematical analysis of the QG equations, particularly regarding the extension of  
 277 recent results on the well-posedness properties for a stochastic RSW model (Crisan & Lang,  
 278 2023) by examining the effect of the QG projector on these properties.

279 This formulation also presents an interesting analogy with the Leray projector formula-  
 280 tion of the Navier-Stokes equations, where the Leray projector enforces the incompressible  
 281 constraint by filtering out compressible sound waves through an elliptic Poisson equation for  
 282 the pressure. Similarly, the proposed QG projector enforces the QG balance by filtering out  
 283 fast gravity waves through an elliptic Helmholtz equation for the PV. It is noteworthy that  
 284 the QG balance is not a constraint added to the RSW model; the Hamiltonian structure of  
 285 the QG model (Holm & Zeitlin, 1998) is distinct from that of the RSW model. Specifically,  
 286 contrary to the pressure, the PV is not a Lagrange multiplier enforcing a constraint.

## 287 4 Numerical experiments

288 This section presents the numerical experiments carried out to validate and explore the  
 289 behavior of our new formulation. We first describe the implementation of the RSW solver  
 290 and QG projector, then detail the specific experiments designed to test vortex shear insta-  
 291 bility, the idealized double-gyre circulation, and a simplified North Atlantic configuration.  
 292 The first two experiments are analyzed to compare the solutions obtained from the QG and  
 293 RSW models under varying conditions and parameters.

### 294 4.1 Numerical implementations

295 To implement our formulation, we require a RSW solver and a QG projector. We  
 296 utilize the RSW solver developed by Roulet and Gaillard (2022), which is available at  
 297 <https://github.com/pvthinker/pyRSW>. We re-implemented this solver in PyTorch to  
 298 enable seamless GPU acceleration, verifying that our implementation reproduces their origi-  
 299 nal results up to numerical precision. The key element of the discretization is a fifth-order  
 300 Weighted Essentially Non-Oscillatory (WENO) upwinded reconstruction for both the mass  
 301 flux and the nonlinear vortex-force term. This approach provides sufficient numerical dis-  
 302 sipation, eliminating the need for an ad-hoc hyperviscous diffusion, while ensuring good  
 303 material conservation of PV (Roulet & Gaillard, 2022).

304 The QG projector requires an elliptic solver. Thiry et al. (2024) released an efficient  
 305 Python-PyTorch implementation of the QG equations. They solve the QG elliptic equation  
 306 using discrete sine transforms implemented with PyTorch’s Fast Fourier Transform (FFT),  
 307 which leverages highly optimized MKL FFT on Intel CPUs and cuFFT on Nvidia GPUs.  
 308 We employ their elliptic solver to solve the QG elliptic equation (11b). Once the projector  
 309 is available, the QG solver is implemented by simply adding the projection step to the RSW  
 310 solver. Numerically, the two solvers differ by only one line of code – the projection step. All  
 311 other elements, including variable staggering, time discretization, and core RSW equations,  
 312 are identical.

313 To summarize, the QG model is advanced in time as follows: (1) compute the RSW  
 314 tendencies, (2) apply the projection operator  $P$  to obtain the QG tendencies, and (3) update  
 315 the state variables. For the RSW model, step (2) is omitted, and only steps (1) and (3) are  
 316 performed.

317 Consequently, we achieve a PyTorch implementation (see Supporting Information files)  
 318 that is concise (approximately 800 lines of code), remains true to the equations, and imple-  
 319 ments both the multi-layer QG and RSW equations using the same state variables ( $\mathbf{u}, \mathbf{v}, \mathbf{h}$ ).

### 320 4.2 Vortex shear instability

321 To validate our formulation, we first study a vortex shear instability and compare its  
 322 evolution in both the QG and the RSW models as  $Ro$  increases for  $Bu = 1$ . The initial state  
 323 is a perfectly shielded vortex with a core of uniform vorticity  $\omega_1$  surrounded by a ring of  
 324 opposite sign uniform vorticity  $\omega_2$ . The system involves two lengths: the core radius  $r_0$  and  
 325 the vortex outer radius  $r_1$ . The ratio  $\omega_2/\omega_1$  is such that the total circulation vanishes. This  
 326 system is unstable and leads to the formation of multipoles (Morel & Carton, 1994). The  
 327 number of poles depends on the ratio of the vortex radius to the core radius. We focus here  
 328 on a tripole formation case with  $r_1/r_0 = 1.4$ . To promote the growth of the most unstable  
 329 mode, we add a small mode azimuthal perturbation.

330 The experiments are set up in dimensional form with a square domain of size  $L_x \times L_y =$   
 331  $100 \text{ km} \times 100 \text{ km}$  on a f-plane. There is a single layer of fluid with thickness  $H = 1 \text{ km}$ . We  
 332 assume no-flow and free-slip boundary conditions. The acceleration of gravity is set to  
 333  $g = 10 \text{ m s}^{-2}$ . The vortex core has a radius  $r_0 = 10 \text{ km}$  and a positive vorticity; the vortex  
 334 radius is  $r_1 = 14 \text{ km}$ . We run the simulations on a  $512 \times 512$  grid, providing a 200m spatial

335 resolution. The Coriolis parameter is chosen such that  $Bu = 1$ , *i.e.*,  $f_0 = \sqrt{gH}/r_0$ . The  
 336 vorticity  $\omega_1$  is set indirectly via  $u_{\max}$ , the maximum velocity of the initial condition. We  
 337 define the Rossby number as  $Ro = u_{\max}/(f_0 r_0)$ . We impose  $Ro$  and deduce  $u_{\max}$ . We have  
 338 tested four cases:  $Ro \in \{0.01, 0.05, 0.1, 0.5\}$ . In all cases, we apply the QG projector to  
 339 the initial state before starting the time integration. Consequently, the initial states are  
 340 in geostrophic balance and differ only by a scaling factor. As  $Ro$  increases, the instability  
 341 develops faster in dimensional time. Therefore, we present the results in the rescaled eddy-  
 342 turnover time  $\tau$ , defined as the inverse of the  $\ell^2$ -norm of the initial vorticity, *i.e.*,  $\tau = 1/\|\omega\|$ .  
 343 We integrate the simulations for  $T = 10\tau$ .

344 Figure 2 shows the evolution of the initial state for the two extreme cases,  $Ro = 0.01$  and  
 345  $Ro = 0.5$ . In the  $Ro = 0.01$  case, the differences between the QG and the RSW solutions are  
 346 not perceptible to the naked eye. This is consistent with the QG scaling and the fact that the  
 347 QG model is an asymptotic limit of the RSW model. In the  $Ro = 0.5$  case, the differences  
 348 are of order one. In the RSW model, the vortex spins faster, and the filaments of negative  
 349 vorticity are stabilized. The smoothness of the RSW solution at  $t = 10\tau$  might be surprising  
 350 as we expect some gravity waves generated during the fast cyclo-geostrophic adjustment of  
 351 the initial state. These gravity waves are present but at  $t = 10\tau$ , they have bounced back  
 352 and forth several times along the boundary and are strongly scattered. Interestingly, the  
 353 QG solution is exactly the same as in the  $Ro = 0.01$  case. This is expected since the QG  
 354 equations are scaling invariant, *i.e.*, the evolution is invariant under multiplication by a  
 355 constant. However, it is also quite remarkable to recover this property in the numerical  
 356 solutions because the QG solver relies on the full RSW right-hand side. Another symmetry  
 357 of the QG model is parity invariance. The solution should be invariant under a sign change  
 358 of the vorticity. In other words, cyclones and anticyclones follow the same evolution, up to  
 359 a change in rotation. This is not at all the case for the RSW model. By flipping the sign  
 360 of the initial vorticity, we verified that the solutions satisfy this property (not shown). This  
 361 means that the QG projector behaves well as it restores two invariances, scaling and parity,  
 362 that are absent in the RSW solver.

363 To assess the influence of  $Ro$  on the time evolution, we define the normalized difference  
 364  $\delta = 2\|\omega_{\text{qg}} - \omega_{\text{sw}}\|/(\|\omega_{\text{qg}}\| + \|\omega_{\text{sw}}\|)$ . Figure 3 shows  $\delta(t)$  for the four  $Ro$  cases. The  
 365 oscillations during the  $[0, 4\tau]$  period are due to the gravity waves in the RSW case resulting  
 366 from the imperfect initial balance. Interestingly, the shortening of the oscillation period as  
 367  $Ro$  decreases is due to the time rescaling by  $\tau$ . In dimensional time, the periods are the  
 368 same. A practical consequence is that the RSW experiment requires more time steps to  
 369 reach  $t = 10\tau$  as  $Ro$  decreases, whereas for the QG experiment, the number of time steps  
 370 is constant. After  $t = 4\tau$ , the differences are dominated by the shear instability developing  
 371 on the vortex. The small difference seen in the snapshots in the  $Ro = 0.01$  case has actually  
 372 reached a plateau, meaning the QG solution closely follows the RSW one. This confirms  
 373 that the QG model is a good simplified model when the scaling assumption holds. On a  
 374 longer time scale and with chaotic vortex dynamics, the solutions would diverge, but in  
 375 such a simple setup, the solutions remain close. The time evolution of  $\delta$  is similar for all  
 376  $Ro$  except  $Ro = 0.5$ , where  $\delta$  saturates at one, the maximum value of this metric. In  
 377 this case, this metric suggests that the two models predict a completely different solution.  
 378 Looking back at the snapshots, this seems exaggerated. The order one difference is mostly  
 379 due to the difference in timing, not the difference in pattern. Depending on the purpose,  
 380 the QG solution might still be of interest as it still captures the main phenomenology. Note  
 381 that the QG solution could be made closer to the RSW solution if the two models were  
 382 started with different initial states: a cyclo-geostrophic balance for the RSW model and  
 383 the associated projected state for the QG model. The initial state would thus depend on  
 384  $Ro$ . For this illustrative experiment, we preferred to stick to the same initial state, up to a  
 385 scaling constant.

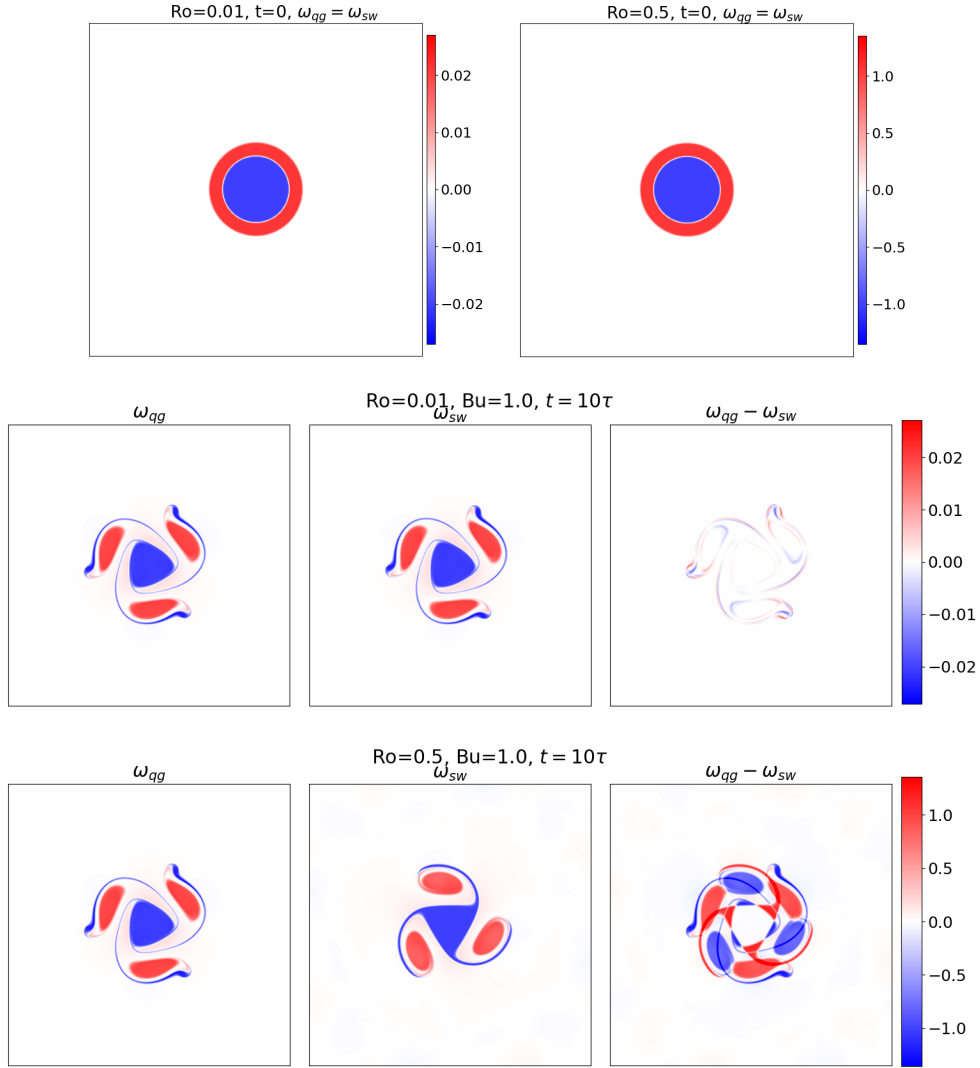


**Figure 2.** Vortex shear instability solved using QG and SW for  $Bu = 1$ . (Top to bottom) Initial relative vorticity for  $Ro = 0.01$  and  $Ro = 0.5$ . Final relative vorticities and their differences for QG and SW models with  $Ro = 0.01$ . Final relative vorticities and their differences for QG and SW models with  $Ro = 0.5$ . Units are in  $s^{-1}$ .

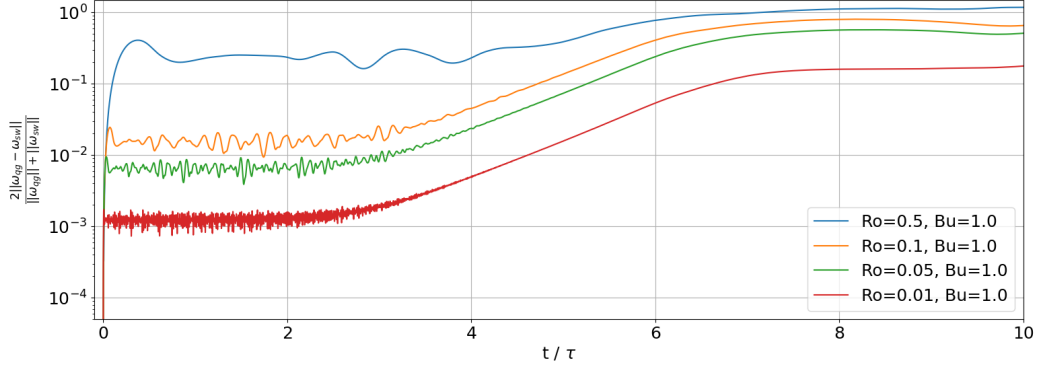


**Figure 3.** Time evolution of the normalized differences of relative vorticity between the QG model and the RSW model with  $Bu = 1$  and different  $Ro$ .

Parameter	Value	Description
$L_x, L_y$	5120, 5120 km	Domain size
$H_k$	400, 1100, 2600 m	Mean layer thickness
$g'_k$	9.81, 0.025, 0.0125 $\text{m s}^{-2}$	Reduced gravity
$\gamma$	$3.6 \cdot 10^{-8} \text{ s}^{-1}$	Bottom drag coefficient
$\tau_0$	$0.08 \text{ N m}^{-2}$	Wind stress magnitude
$\rho$	$1000 \text{ kg m}^{-3}$	Ocean density
$f_0$	$9.375 \cdot 10^{-5} \text{ s}^{-1}$	Mean Coriolis parameter
$\beta$	$1.754 \cdot 10^{-11} (\text{m s})^{-1}$	Coriolis parameter gradient
$L_d$	41, 25 km	Baroclinic Rossby radii
$n_x, n_y$	256, 256	Grid size
$dt$	4000 s	Time-step

**Table 1.** Parameters of the idealized double-gyre configuration. There no viscosity nor diffusion coefficient as the grid-scale dissipation is implicitly handled by the upwinded WENO reconstruction of the mass flux and the vortex-force (see Roulet & Gaillard, 2022).

### 4.3 Double-gyre circulation

To explore a richer phenomenology, we have tested our new formulation on a classical oceanic test case, the idealized wind-forced double-gyre circulation. The domain is a non-periodic square ocean basin with  $N = 3$  layers. We assume free-slip boundary conditions on each boundary. A stationary and symmetric wind stress  $(\tau_x, \tau_y)$  is applied in the top layer, with  $\tau_x = -(\tau_0/\rho_0) \cos(2\pi y/L_y)$  and  $\tau_y = 0$ . Additionally, a linear drag with drag coefficient  $\gamma$  is applied in the bottom layer. The parameter values are given in Table 1.

We study this configuration in an eddy-permitting resolution of 20 km, meaning that the spatial resolution (20 km) is half of the largest baroclinic Rossby radius (41 km). We expect QG and RSW simulations to produce strong western boundary currents converging to the middle of the western boundary and an eastward jet departing from the middle of the western boundary. Starting from the rest state, this configuration requires about 100 years to spin up and achieve converged statistics (Hogg et al., 2005; Simonnet, 2005).

In Figure 4, we present snapshots of key quantities of the upper layer after 100 years of integration. The solution exhibits expected properties of this setup: a double-gyre circulation (Fig. 4e) separated by a meandering eastward jet (Fig. 4a,d) emanating from the western boundary, two strong and narrow western boundary currents (Fig. 4b) feeding the eastward

403 jet, mesoscale turbulence throughout, especially near the jet (Fig. 4c,d), and Rossby waves  
 404 propagation (Fig. 4e,f). The local Rossby number, defined as  $\omega/f_0$  peaks at 0.2, which is  
 405 significant but not large enough to dismiss the solution. Interestingly, the layer thickness  
 406 perturbation  $h_1$  is substantial compared to the reference depth  $H_1 = 400$  m.

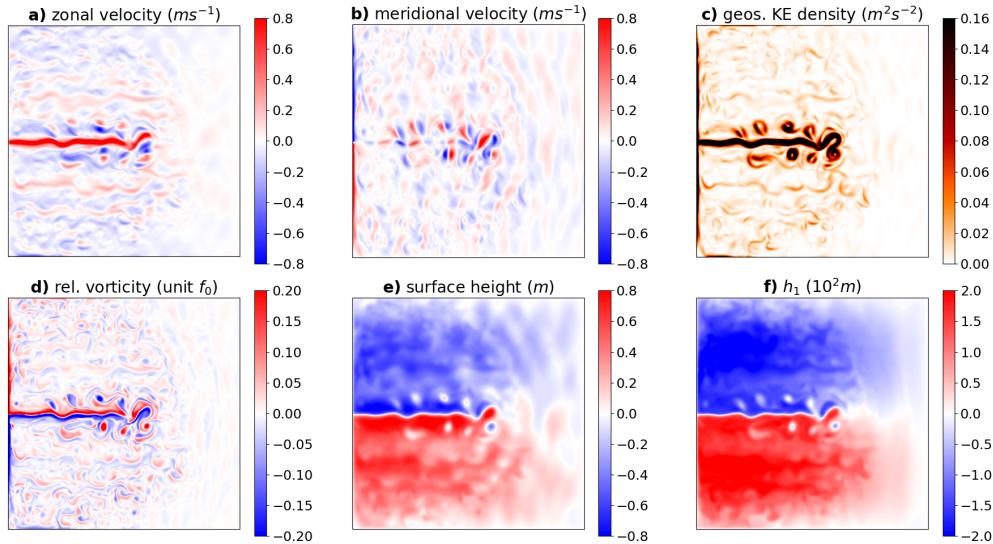


**Figure 4.** QG upper-layer snapshot after 100 years of spin-up from the rest state. KE, geos., and rel. stand for kinetic energy, geostrophic, and relative, respectively.

407 To complement this snapshot, we present statistics estimated over the years (100-200)  
 408 after the initial state, using one snapshot every 10 days. We decompose the geostrophic  
 409 kinetic energy into its mean and eddy components, and compute the ratio  $k_a/k_g$ . The  
 410 results are shown in Figure 5 for the upper layer. The statistics confirm the presence of the  
 411 strong western boundary currents (Fig. 5a) and a strong eastward jet reaching the middle of  
 412 the domain (Fig. 5a,d). A remarkable feature is the symmetry of all quantities with respect  
 413 to the central latitude, due to the symmetry of the forcing and the cyclone/anticyclone  
 414 symmetry of the QG model. This symmetry prevents the model from breaking the symmetry  
 415 of the forcing. From the ratio  $k_a/k_g$  and  $h/H$  (Fig. 5c,f), we test the validity of the QG  
 416 scaling assumptions (Eq. 23). The color scale is adjusted so that the white intermediate  
 417 color corresponds to  $Ro = 0.1$ . Red areas indicate where the QG scaling assumptions are not  
 418 respected. Counter-intuitively, the central jet region, where kinetic energy is the highest,  
 419 shows the best QG scaling. The worst regions are the gyre centers due to large thickness  
 420 deviations and the boundaries due to large ageostrophic velocities.

421 Finally, we compare the QG solution with its companion RSW one. Due to the  
 422 free surface and the presence of fast barotropic gravity waves, the RSW solver requires  
 423 a much smaller time step, typically 200 times smaller. This factor corresponds to the ratio  
 424  $\sqrt{gH}/\max(u)$ . Integrating from the rest state over 200 years would be computationally  
 425 intensive. A compromise would be to use a barotropic-baroclinic time splitting (Higdon &  
 426 De Szoeke, 1997) or implicit stepping of the free surface (Roullet & Madec, 2000), but this  
 427 is beyond the scope of the present study. Instead, we ran the RSW solver starting from year  
 428 200 of the QG solution and integrate it over 2 years. Figure 6 compares QG and RSW on  
 429 a snapshot of vorticity in the upper layer. The central jet has a southward component, the  
 430 two gyres are no longer symmetric, and mesoscale turbulence has intensified in the Northern  
 431 gyre and weakened in the Southern gyre. Applying the QG projector on the RSW state  
 432 results in a state that remains very close (Fig. 6c) yet with damped fluctuations. The QG

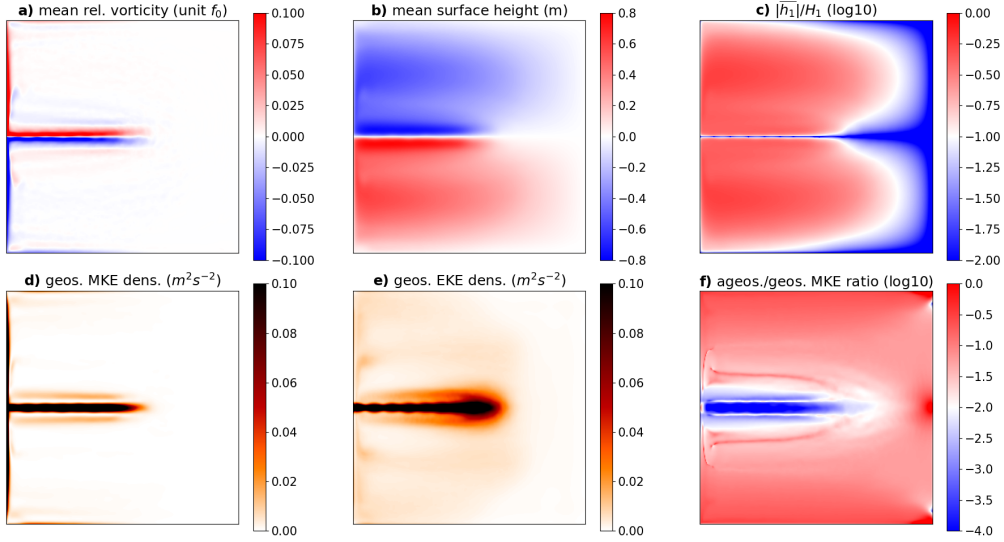


**Figure 5.** QG upper-layer statistics over 100 years after 100 years spin-up from rest state.

433 projector tends to dampen the short scales, but since it is applied on the RSW model ten-  
 434 dency, it does not affect the QG state, as seen from the comparison between Fig. 6a and  
 435 Fig. 6b. The closeness suggests that while the QG solution might be locally tangent to the  
 436 RSW solution, long-term integration results in noticeable differences.

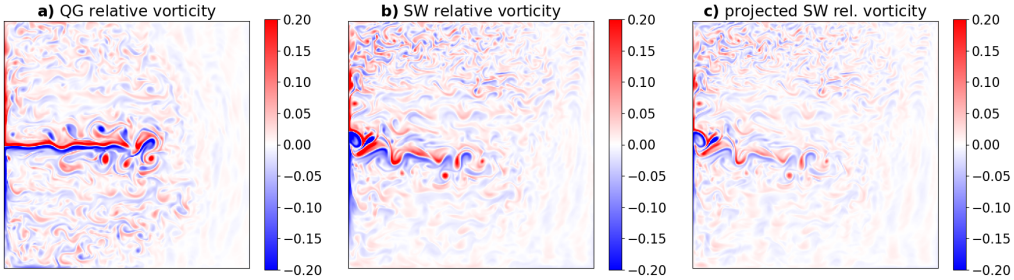


**Figure 6.** (Left) QG upper-layer relative vorticity after 100 years of spin-up, (middle) RSW  
 upper-layer relative vorticity, and (right) projected RSW vorticity after 2 additional years of spin-  
 up. Units are in  $f_0$ .

437 **4.4 Simplified North Atlantic configuration**

438 To demonstrate the applicability of the proposed projection formulation to more com-  
 439 plex ocean configurations, we extend the previous idealized double-gyre circulation to the  
 440 North Atlantic basin, located at  $9^\circ\text{N}$ – $48^\circ\text{N}$  and  $98^\circ\text{W}$ – $4^\circ\text{W}$ . The ocean boundaries are set  
 441 at a depth of 250 meters to exclude the continental shelf from the simulation. In this study,  
 442 we simplify the realistic North Atlantic configuration by not considering inflows and out-  
 443 flows across the northern and southern open boundaries (Marchesiello et al., 2001; Blayo &  
 444 Debreu, 2005), which will be investigated in subsequent studies. Here, we assume a flat bot-  
 445 tom to be consistent with the formulation presented in the previous sections. However, the  
 446 presented formulation could be extended to include bottom topography in the future. The

447 ocean surface boundary condition is imposed using the Hellerman and Rosenstein (1983)  
 448 monthly wind stress climatology, which has been widely used in several other reference  
 449 simulations of the Gulf Stream (Blayo et al., 1994; Hurlburt & Hogan, 2000).

450 The simulation runs on a horizontal grid of  $1024 \times 512$  points, corresponding to a spatial  
 451 resolution of 8.5 km ( $\sim 1/11^\circ$ ), with 3 vertical layers using the same reference thickness and  
 452 reduced gravity as specified in Table 1. The time step is set to 2000 s, and a partial free-slip  
 453 condition is applied on the ocean boundaries with the coefficient set to 0.6 (0 for no-slip  
 454 and 1 for free-slip). To solve the elliptic equation on non-rectangular geometries for the QG  
 455 projector, we extend the fast discrete sine transform spectral solver using the capacitance  
 456 matrix method (Thiry et al. (2024), see also Blayo and LeProvost (1992) for the original  
 457 technique).

458 Figure 7 illustrates the instantaneous prognostic and diagnostic variables of the pro-  
 459 jected QG model after 40 years of spin-up simulation. The surface relative vorticity in  
 460 Fig. 7a reveals the meandering and energetic western boundary current, along with the tur-  
 461 bulent eddying structures throughout most of the basin. The sea surface height in Fig. 7b  
 462 illustrates the gyre circulation structure in this configuration and could potentially be as-  
 463 similated with available observations. Fig. 7c and Fig. 7d demonstrate the surface current  
 464 speed ( $\sqrt{u_1^2 + v_1^2}$ ) for the prognostic geostrophic motions and the diagnostic ageostrophic  
 465 motions, respectively. The latter is at least five times smaller than the former across the  
 466 entire basin. This instantaneous snapshot notably shows that the ageostrophic velocity  
 467 component is extremely small in the region going from  $25^\circ\text{N}$  to  $30^\circ\text{N}$ , which approximately  
 468 corresponds to the range of latitudes for the state of Florida. However, the ageostrophic  
 469 motions remain significant along the Gulf Stream current.

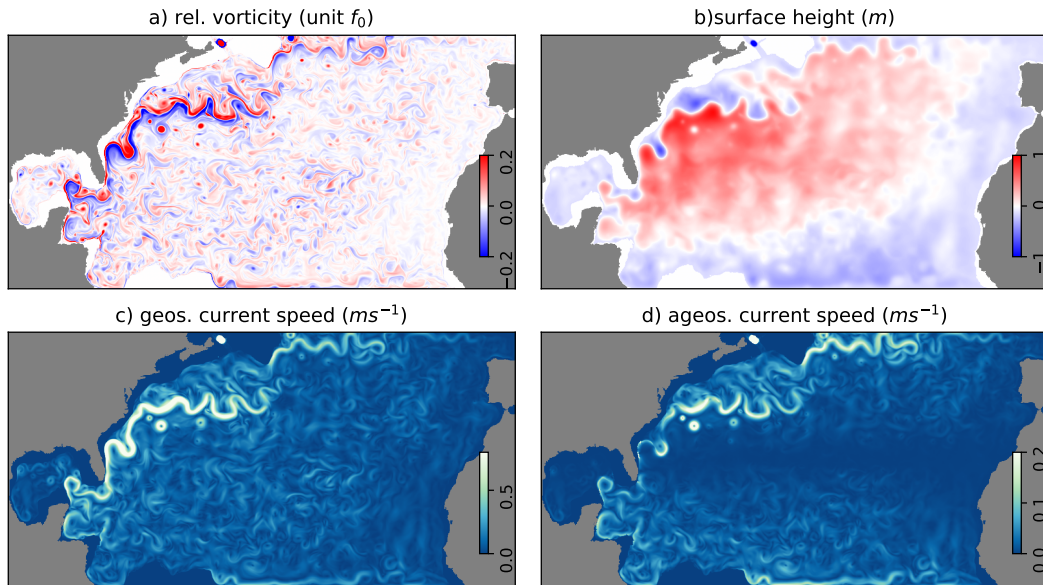


**Figure 7.** QG upper-layer snapshot after 40 years of spin-up from the rest state.

470 We also investigate the temporal statistics of the projected QG model over 20 years  
 471 following a 40-year spin-up. For instance, Figure 8 illustrates the surface MKE and EKE  
 472 densities for both geostrophic and ageostrophic motions. Figures 8a and 8b reveal that EKE  
 473 predominates over MKE across the basin, particularly along the Gulf Stream, highlighting  
 474 the significant influence of mesoscale eddies on flow variability. Figures 8c and 8d show the  
 475 ratio of ageostrophic to geostrophic MKE and EKE, confirming the previous instantaneous

476 finding: geostrophic balance is markedly dominant in the North Atlantic Subtropical Gyre,  
 477 validating the QG scaling in that region.

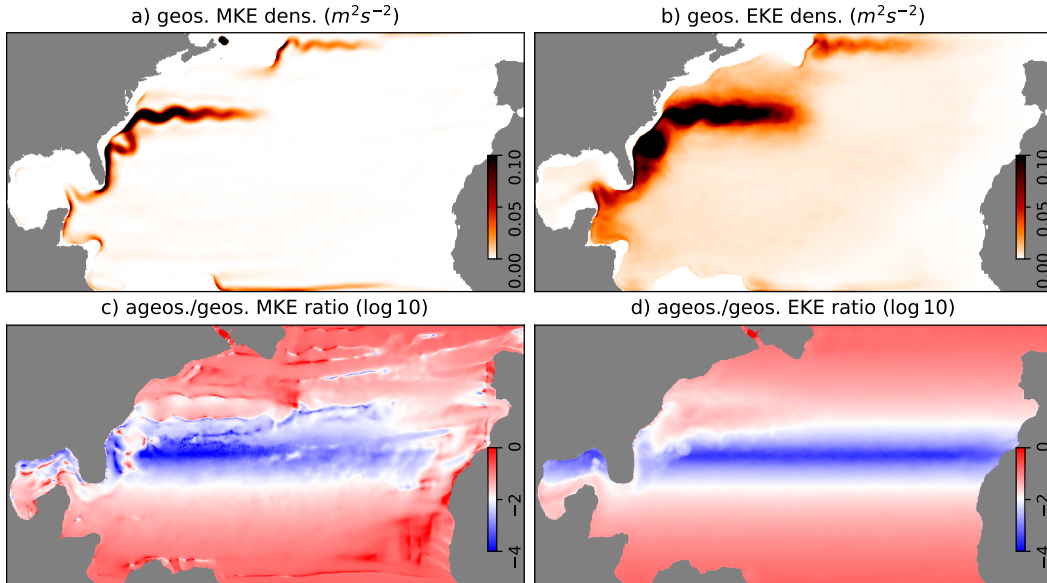


**Figure 8.** QG upper-layer statistics over 20 years after 40 years spin-up from rest state.

## 478 5 Conclusions

479 In this paper, we have demonstrated that the QG model can be formulated as a pro-  
 480 jected RSW model by applying the QG projector  $P$  (defined in Equation 16) to the RSW  
 481 tendency. This formulation allows the QG model to utilize the same variables ( $\mathbf{u}$ ,  $\mathbf{v}$ ,  $\mathbf{h}$ ) as  
 482 the RSW model, rather than the more conventional ( $\mathbf{p}$ ,  $\mathbf{q}$ ) variables. This unified approach  
 483 enables us to enhance the similarities and differences between the two models and facilitates  
 484 a coherent integration of both models within the same numerical framework. In contrast to  
 485 earlier approaches based on similar concepts (Leith, 1980; Salmon, 1998; Saujani & Shep-  
 486 herd, 2006), the projection formulation we propose here does not depend on the shape of the  
 487 boundary. As demonstrated, it can be easily implemented for basins with general coastal  
 488 geometries.

489 We have validated this approach through a vortex shear instability test, demonstrating  
 490 that the resulting QG model retains essential symmetry properties, such as scaling and  
 491 parity, which are not present in the RSW model. Furthermore, we have shown that a QG  
 492 model implemented in this manner reproduces the expected characteristics of a double-gyre  
 493 experiment. An immediate benefit of this approach is the ability to directly compare RSW  
 494 and QG solutions. This straightforward formulation paves the way for further investigations  
 495 into the differences between QG and RSW equations, such as studies on the stability of  
 496 geostrophic equilibrium or spontaneous imbalance phenomena.

497 Additionally, it holds significant potential for data assimilation applications, enabling  
 498 seamless switching between these nested RSW and QG models or even their combination.  
 499 For instance, one could initially run a data assimilation algorithm, such as an ensemble  
 500 Kalman filter (Evensen, 2003), using the projected QG model to capture geostrophic dy-  
 501 namics. Subsequently, the obtained solution could be refined by transitioning to the RSW  
 502 model. This flexibility could enhance the accuracy and efficiency of data assimilation pro-  
 503 cesses in oceanographic modeling and related fields.

## Open Research Section

The code files necessary to reproduce the results presented in this paper are publicly available in Thiry and Li (2024).

## Acknowledgments

The authors gratefully acknowledge the two anonymous reviewers for their insightful comments and suggestions, which helped to significantly improve the manuscript. We also wish to acknowledge the support of the ERC EU project 856408-STUOD, which enabled the research presented in this paper. Additionally, the authors extend their thanks to Anne-Laure Dalibard for her invaluable contribution in directing them to Frederic Charve's Thesis. Furthermore, the authors express their gratitude to Frederic Charve for engaging discussions.

## References

- Bachman, S. (2019). The GM+E closure: a framework for coupling backscatter with the Gent and McWilliams parameterization. *Ocean Modelling*, *136*, 85–106.
- Bachman, S., Fox-Kemper, B., & Pearson, B. (2017). A scale-aware subgrid model for quasi-geostrophic turbulence. *Journal of Geophysical Research: Oceans*, *122*, 1529–1554.
- Bauer, W., Chandramouli, P., Chapron, B., Li, L., & Mémin, E. (2020). Deciphering the role of small-scale inhomogeneity on geophysical flow structuration: A stochastic approach. *Journal of Physical Oceanography*, *50*, 983–1003.
- Berloff, P. (2005). Random-forcing model of the mesoscale oceanic eddies. *Journal of Fluid Mechanics*, *529*, 71–95.
- Blayo, E., & Debreu, L. (2005). Revisiting open boundary conditions from the point of view of characteristic variables. *Ocean Modelling*, *9*(3), 231–252.
- Blayo, E., & LeProvost, C. (1992, 10). Performance of the capacitance matrix method for solving Helmholtz-type equations in ocean modelling. *Journal of Computational Physics*, *102*.
- Blayo, E., Verron, J., & Molines, J. M. (1994). Assimilation of TOPEX/POSEIDON altimeter data into a circulation model of the North Atlantic. *Journal of Geophysical Research: Oceans*, *99*(C12), 24691–24705.
- Bourgeois, A., & Beale, J. (1994). Validity of the quasigeostrophic model for large-scale flow in the atmosphere and ocean. *SIAM Journal on Mathematical Analysis*, *25*(4), 1023–1068.
- Charve, F. (2004). *Etude de phénomènes dispersifs en mécanique des fluides géophysiques* (Unpublished doctoral dissertation). Palaiseau, Ecole polytechnique.
- Crisan, D., & Lang, O. (2023). Well-posedness properties for a stochastic rotating shallow water model. *Journal of Dynamics and Differential Equations*, 1–31.
- Cushman-Roisin, B., & Beckers, J. (2011). *Introduction to geophysical fluid dynamics: physical and numerical aspects*. Academic Press.
- Dutton, J. (1974). The nonlinear quasi-geostrophic equation: Existence and uniqueness of solutions on a bounded domain. *Journal of Atmospheric Sciences*, *31*(2), 422–433.
- Evensen, G. (2003). The ensemble Kalman filter: Theoretical formulation and practical implementation. *Ocean Dynamics*, *53*, 343–367.
- Grooms, I., Majda, A., & Smith, K. (2015). Stochastic superparameterization in a quasi-geostrophic model of the Antarctic Circumpolar Current. *Ocean Modelling*, *85*, 1–15.
- Hellerman, S., & Rosenstein, M. (1983). Normal monthly wind stress over the world ocean with error estimates. *Journal of Physical Oceanography*, *13*, 1093–1104.
- Higdon, R., & De Szoeke, R. (1997). Barotropic-baroclinic time splitting for ocean circulation modeling. *Journal of Computational Physics*, *135*(1), 30–53.

- 553 Hogg, A., Killworth, P., Blundell, J., & Dewar, W. (2005). Mechanisms of decadal variability  
554 of the wind-driven ocean circulation. *Journal of Physical Oceanography*, *35*(4), 512–  
555 531.
- 556 Holm, D. D., & Zeitlin, V. (1998). Hamilton’s principle for quasigeostrophic motion. *Physics*  
557 *of fluids*, *10*(4), 800–806.
- 558 Holton, J. (1973). An introduction to dynamic meteorology. *American Journal of Physics*,  
559 *41*(5), 752–754.
- 560 Hurlburt, H. E., & Hogan, P. J. (2000). Impact of  $1/8^\circ$  to  $1/64^\circ$  resolution on Gulf Stream  
561 model–data comparisons in basin-scale subtropical Atlantic ocean models. *Dynamics*  
562 *of Atmospheres and Oceans*, *32*(3), 283–329.
- 563 Jansen, M., & Held, I. (2014). Parameterizing subgrid-scale eddy effects using energetically  
564 consistent backscatter. *Ocean Modelling*, *80*, 36–48.
- 565 Leith, C. E. (1980). Nonlinear normal mode initialization and quasi-geostrophic theory.  
566 *Journal of the Atmospheric Sciences*, *37*, 958–968.
- 567 Li, L., Deremble, B., Lahaye, N., & Mémin, E. (2023). Stochastic data-driven parameter-  
568 ization of unresolved eddy effects in a baroclinic quasi-geostrophic model. *Journal of*  
569 *Advances in Modeling Earth Systems*, *15*(2), e2022MS003297.
- 570 Marchesiello, P., McWilliams, J. C., & Shchepetkin, A. (2001). Open boundary conditions  
571 for long-term integration of regional oceanic models. *Ocean Modelling*, *3*(1), 1–20.
- 572 Marshall, D., Maddison, J., & Berloff, P. (2012). A framework for parameterizing eddy  
573 potential vorticity fluxes. *Journal of Physical Oceanography*, *42*(4), 539–557.
- 574 McWilliams, J. (2006). *Fundamentals of geophysical fluid dynamics*. Cambridge University  
575 Press.
- 576 McWilliams, J. C. (1977). A note on a consistent quasigeostrophic model in a multiply  
577 connected domain. *Dynamics of Atmospheres and Oceans*, *1*(5), 427–441.
- 578 Morel, Y., & Carton, X. (1994). Multipolar vortices in two-dimensional incompressible  
579 flows. *Journal of Fluid Mechanics*, *267*, 23–51.
- 580 Paszke, A., Gross, S., Massa, F., Lerer, A., Bradbury, J., Chanan, G., ... others (2019).  
581 Pytorch: An imperative style, high-performance deep learning library. *Advances in*  
582 *Neural Information Processing Systems*, *32*.
- 583 Pedlosky, J. (2013). *Geophysical fluid dynamics*. Springer Science & Business Media.
- 584 Roulet, G., & Gaillard, T. (2022). A fast monotone discretization of the rotating  
585 shallow water equations. *Journal of Advances in Modeling Earth Systems*, *14*(2),  
586 e2021MS002663.
- 587 Roulet, G., & Madec, G. (2000). Salt conservation, free surface, and varying levels: a new  
588 formulation for ocean general circulation models. *Journal of Geophysical Research:*  
589 *Oceans*, *105*(C10), 23927–23942.
- 590 Salmon, R. (1998). *Lectures on geophysical fluid dynamics*. Oxford Academic.
- 591 Saujani, S., & Shepherd, T. G. (2006). A unified theory of balance in the extratropics.  
592 *Journal of Fluid Mechanics*, *569*, 447–464.
- 593 Simonnet, E. (2005). Quantization of the low-frequency variability of the double-gyre  
594 circulation. *Journal of Physical Oceanography*, *35*(11), 2268–2290.
- 595 Thiry, L., & Li, L. (2024). *A unified formulation of quasi-geostrophic and shallow water*  
596 *equations via projection*. Zenodo. Retrieved from [https://doi.org/10.5281/zenodo](https://doi.org/10.5281/zenodo.13372736)  
597 [.13372736](https://doi.org/10.5281/zenodo.13372736) ([Software])
- 598 Thiry, L., Li, L., Roulet, G., & Mémin, E. (2024). MQGeometry-1.0: a multi-layer quasi-  
599 geostrophic solver on non-rectangular geometries. *Geoscientific Model Development*,  
600 *17*(4), 1749–1764.
- 601 Uchida, T., Deremble, B., & Popinet, S. (2022). Deterministic model of the eddy dynamics  
602 for a midlatitude ocean model. *Journal of Physical Oceanography*, *52*(6), 1133–1154.
- 603 Vallis, G. (2017). *Atmospheric and oceanic fluid dynamics*. Cambridge University Press.
- 604 Zanna, L., Mana, P., Anstey, J., David, T., & Bolton, T. (2017). Scale-aware deterministic  
605 and stochastic parametrizations of eddy-mean flow interaction. *Ocean Modelling*, *111*,  
606 66–80.

607 Zeitlin, V. (2018). *Geophysical fluid dynamics: understanding (almost) everything with*  
608 *rotating shallow water models*. Oxford University Press.